Supporting Information

Bi/ZIF-8 catalysts: the important role of ZIF-8 for enhanced electrochemical N_2-to-NH_3 conversion in neutral electrolyte

Pengju Guo, Fengxiang Yin, Jiahui Liang*

Jiangsu Key Laboratory of Advanced Catalytic Materials and Technology, School of Petrochemical Engineering, Changzhou University, Changzhou 213164, PR China

**Corresponding author*

Tel.: +86-519-86330253

E-mail address: yinfx@cczu.edu.cn (F. Yin)

1. Experimental section

1.1. Characterizations

X-ray powder diffraction (XRD) was performed on a Smartlab 9 diffractometer (Rigaku, Japan) with Cu Kα radiation (λ = 1.5406 Å). Scanning electron microscope (SEM) was taken at (Zeiss gemini360, Germany). The morphology was observed by transmission electron microscopy and high-resolution transmission electron microscope (TEM/ HRTEM, FEI Tecnai G2 F20, Thermo Fisher Scientific). And the X-ray energy spectrum scan analysis (EDX mapping) were perLformed on the TEM electron microscope. Specific surface areas and the pore size distribution were determined using Brunauer-Emmett-Teller (BET) method and Horvath-Kawazoe (HK) method, respectively. X-ray photoelectron spectroscopy (XPS) was carried out on Escalab 250 Xray photoelectron spectrometer (Thermfisher Scientific, USA) equipped with an Al-Ka source and 30 eV passing energy.

1.2. Preparation of ZIF-8

First, $Zn(NO_3)_2 \cdot 6(H_2O)$ (5 mmol) and 2-methylimidazole (12 mmol) were dispersed into methanol solution (40 mL) and stirred to obtain a clarified precursor solution. Then, this solution was sealed at room temperature and kept undisturbed for 6 h to obtain the white product ZIF-8.

2. Electrochemical measurements

2.1. NRR tests

NRR tests were conducted at room temperature using H-type electrolysis cell. Electrochemical tests were performed using a standard three-electrode, where Pt served

as the counter electrode, Ag/AgCl (3.5 M KCl) as the reference electrode, and membrane electrode assembly (MEA) as the working electrode. The electrolyte volume of anode chamber are both 45 mL Na_2SO_4 (0.1 mol L^{-1}). After purging with ultra-high purity N_2 (99.999%) for 30 minutes, the N_2 reduction test was conducted. During the whole electrolysis process, the gas flow rate of N_2 was kept constant at 20 mL min^{-1}. Linear sweep voltammetry (LSV) was performed at 5 mV s^{-1} in the N_2 or Ar filled states, respectively. The NRR performance was evaluated at different potentials by chronoamperometry (*i-t*). Electrochemical impedance (EIS) was tested in the frequency range of 10^{-1} to 10^6 Hz under open-circuit voltage (OCP). Cyclic voltammetry (CV) was performed at different scan rates near OCP to obtain the electric double layer capacitance (C_{dl}), which was proportional to the electrochemically active surface area (ECSA). All potentials in this paper are based on the reversible hydrogen electrode (RHE), see **Equation (1)**:

$$E_{(RHE)} = E_{(Ag/AgCl)} + 0.059 \times PH + 0.179 \quad (1)$$

2.2. Preparation of the working electrode

The electrocatalyst (8 mg) and carbon black (8 mg) were dispersed in a solution containing ethanol (0.9 mL) and Nafion (0.1 mL, 5 wt%, DuPont), which was then sonicated to obtain uniform ink mixing liquid. Finally, about 62.34 μL of ink was dropped onto a clean carbon paper (CP) (1 × 1 cm^2), and dried naturally to obtain the working electrode. The loading amount of the electrocatalyst was 0.5 mg cm^{-2}.

2.4. C_{dl} and ECSA tests

Electrochemical active surface area (ECSA) is the effective area of the catalyst

involved in the electrochemical reaction. Increased ECSA contributes to the exposure of more active sites. ECSA was derived from C_{dl}. The relationship between C_{dl} and ECSA is proportional. Generally, the higher the value of C_{dl}, the better the activity of the catalytic material. So, C_{dl} can be used to evaluate the relative size of ECSA.

Equation (2) was used to calculate C_{dl}:

$$C_{dl} = Slope/2 \quad (2)$$

where C_{dl} is a double layer capacitor; Slope is the linear ratios of the current density differences and different scanning rates (10, 20, 30, 40, 50 mV/s) in the non-Faraday zone.

3. Determination of products

3.1. Determination of ammonia

The indophenol blue method was used to determine the production of NH_3. After the NRR test was completed, 5 mL of the solution was taken from the cathode chamber and transferred to a 10 mL colorimetric tube. Then, 1 mL of chromogenic reagent (containing 0.375 mol L^{-1} NaOH, 0.36 mol L^{-1} salicylic acid and 0.18 mol L^{-1} sodium potassium tartrate), 100 uL of NaOH solution containing NaClO (0.75 mol L^{-1}, 100 μL) (the concentration of Cl is 3.5 g L^{-1}) and 100 uL sodium nitrosoferricyanide solution (1wt%, 100 μL) were added to the colorimetric tube. Finally, the above mixed solution was diluted to 10 mL with deionized water. After standing for 1 h away from light, the absorbance of the mixture at 697 nm was measured using a UV-Vis spectrophotometer (Agilent, Cary 60 UV-Vis). Using a series of concentrations of ammonium chloride (NH_4Cl) standard solution to calibrate the concentration-absorbance and then to draw a

fitting standard curve to determine the amount of NH_3 produced. The standard curve takes the absorbance value at 697 nm wavelength as the y-axis, and the NH_3 concentration as x. The obtained standard curve is y = 0.63161x + 0.06589, R^2 = 0.9994, which shows that the absorbance value and the NH_3 concentration have a good linear relationship.

3.2. Determination of hydrazine

The Watt-Chrisp method was used to determine the concentration of the by-product N_2H_4 A mixed solution containing p-(dimethylamino)benzaldehyde (4 g), concentrated hydrochloric acid (20 mL) and ethanol (200 mL) was used as chromogenic reagent. After the NRR test was completed, 1 mL of solution was taken from the cathode chamber and added to a 10 mL colourimetric tube, followed by 2 mL chromogenic reagent. Subsequently, the above mixture was diluted to 10 mL with 1 mol L^{-1} HCl. After standing for 20 min away from light, the absorbance at 458 nm was measured in UV. Using a series of concentrations of hydrazine hydrochloride standard solution to calibrate the concentration-absorbance and then to draw a fitting standard curve to determine the amount of by-product N_2H_4. The standard curve takes the absorbance value at 458 nm wavelength as the y-axis, and the N_2H_4 concentration as x. The obtained standard curve is y = 1.5436x+0.00403, R^2 = 0.9992, which shows that the absorbance value and the N_2H_4 concentration have a good linear relationship.

3.3. Calculations of NH_3 yield and faradaic efficiency (FE)

Equation (3) was used to calculate NH_3 yield:

$$Yield_{(NH3)} = C_{(NH3)} \times V/(t \times mg_{cat.}) \quad (3)$$

where V is the volume of the electrolyte (mL), $C_{(NH3)}$ is the measured NH_3 concentration (ug mL^{-1}), $mg_{cat.}$ is the loading mass of the catalyst on the carbon paper, and t is the test time.

Equation (4) was used to calculate FE:

$$FE = C_{(NH3)} \times V \times 3F/(Q \times 17) \times 100\% \quad (4)$$

where V is the volume of the electrolyte (mL), $C_{(NH3)}$ is the measured NH_3 concentration (ug mL^{-1}), F is the Faraday constant (96500 C mol^{-1}), Q is the total charges passed through the electrode (C).

4. Computational details

The density functional theory (DFT) calculations were carried out with the VASP code [S1]. The Perdew–Burke–Ernzerhof (PBE) functional within generalized gradient approximation (GGA) [S2] was used to process the exchange–correlation, while the projectoraugmented-wave pseudopotential (PAW) [S3] was applied with a kinetic energy cut-off of 500 eV, which was utilized to describe the expansion of the electronic eigenfunctions. The vacuum thickness was set to be 20 Å to minimize interlayer interactions. The Brillouin-zone integration was sampled by a Γ-centered 5 × 5 × 1 Monkhorst–Pack k-point. All atomic positions were fully relaxed until energy and force reached a tolerance of 1×10^{-6} eV and 0.01 eV/Å, respectively. The dispersion corrected DFT-D method was employed to consider the long-range interactions [S4].

The Gibbs free energy change (ΔG) was calculated by computational hydrogen electrode (CHE) model as follows **Equation (5)**:

$$\Delta G = \Delta E + \Delta ZPE - T\Delta S \quad (5)$$

where ΔE is the reaction energy of the total energy difference between the reactant and product molecules absorbed on the catalyst surface and ΔS is the change in entropy for each reaction, ΔZPE is the zero-point energy correction to the Gibbs free energy.

Table S1. The pore volumes and the mean pore diameters of the different samples

Samples	Pore volume (cm^3 g^{-1}) /adsorption	Mean pore diameter (nm) /adsorption
ZIF-8	0.591429	2.2774
Bi NPs	0.305694	2.3169
4%Bi/ZIF-8	0.377218	2.5603
8%Bi/ZIF-8	0.455014	2.7818
12%Bi/ZIF-8	0.339901	2.4162

Table S2. C 1s, N 1s, Zn 2p and Bi 4f binding energies of the catalysts determined by XPS.

Samples	C 1s (eV)		N 1s (eV)		Zn 2p (eV)		Bi^{3+} (eV)		Bi^{0} (eV)	
	C-C/C-H	C-N	N-C	N=C	Zn $2p_{1/2}$	Zn $2p_{3/2}$	Bi $4f_{5/2}$	Bi $4f_{7/2}$	Bi $4f_{5/2}$	Bi $4f_{7/}$
ZIF-8	284.6	285.8	398.9	400.3	1044.5	1021.4	/	/	/	/
Bi NPs	/	/	/	/	/	/	164.2	158.9	162.1	156.8
8%Bi/ZIF-8	284.5	285.7	398.8	400.2	1044.8	1021.7	163.9	158.6	161.8	156.5

Table S3. NH_3 yields of the prepared electrocatalysts.

Samples	NH_3 yield (ug h^{-1} $mg^{-1}_{cat.}$)				
	-0.3 V	-0.4 V	-0.5 V	-0.6 V	-0.7 V
ZIF-8	3.01 ± 0.08	4.71 ± 0.06	6.87 ± 0.14	3.43 ± 0.07	2.98 ± 0.06
Bi NPs	4.23 ± 0.07	7.37 ± 0.16	8.86 ± 0.14	5.81 ± 0.11	5.37 ± 0.10
4%Bi/ZIF-8	11.95 ± 0.21	20.28 ± 0.25	26.14 ± 0.31	16.63 ± 0.20	9.38 ± 0.18
6%Bi/ZIF-8	16.72 ± 0.34	22.08 ± 0.41	30.68 ± 0.47	24.06 ± 0.31	13.27 ± 0.33
8%Bi/ZIF-8	19.93 ± 0.35	25.18 ± 0.50	34.53 ± 0.52	30.73 ± 0.52	16.23 ± 0.47
10%Bi/ZIF-8	12.68 ± 0.26	23.57 ± 0.30	27.65 ± 0.41	21.40 ± 0.32	10.96 ± 0.27
12%Bi/ZIF-8	9.68 ± 0.13	19.83 ± 0.19	21.73 ± 0.25	12.09 ± 0.14	7.05 ± 0.14

Table S4. Faradaic efficiencies of the prepared electrocatalysts.

Samples	Faradaic efficiency (%)				
	-0.3 V	-0.4 V	-0.5 V	-0.6 V	-0.7 V
ZIF-8	3.15 ± 0.06	4.87 ± 0.05	5.37 ± 0.12	3.26 ± 0.06	2.07 ± 0.05
Bi NPs	3.37 ± 0.07	7.39 ± 0.11	9.73 ± 0.11	6.86 ± 0.07	4.24 ± 0.08
4%Bi/ZIF-8	9.38 ± 0.15	14.37 ± 0.24	20.29 ± 0.30	12.81 ± 0.25	7.82 ± 0.18
6%Bi/ZIF-8	11.08 ± 0.24	14.69 ± 0.31	21.65 ± 0.35	18.72 ± 0.27	8.02 ± 0.23
8%Bi/ZIF-8	14.73 ± 0.26	16.16 ± 0.37	23.27 ± 0.43	21.69 ± 0.28	11.61 ± 0.28
10%Bi/ZIF-8	11.81 ± 0.14	15.08 ± 0.23	19.83 ± 0.21	13.85 ± 0.21	9.37 ± 0.16
12%Bi/ZIF-8	7.37 ± 0.13	14.19 ± 0.13	16.26 ± 0.17	10.79 ± 0.17	8.64 ± 0.14

Table S5. The reported NRR activity of the Bismuth based electrocatalysts.

Catalysts	Electrolyte	NH_3 yield ($ug\ h^{-1}\ mg^{-1}_{cat.}$)	FE (%)	Refs.
8%Bi/ZIF-8	0.1 M Na_2SO_4	34.53	23.27	This work
Bi@C nanosheets	0.1 M Na_2SO_4	4.22	15.1	S5
B doped Bi nanoroll	0.05 M H_2SO_4	29.2	8.3	S6
β-Bi_2O_3	0.1 M Na_2SO_4	19.92	4.3	S7
$Bi_4V_2O_{11}/CeO_2$	0.2 M Na_2SO_4	23.21	10.16	S8
OVs $BiVO_4$	0.1 M KOH	8.6	10.04	S9
Plasma R-O-Bi	0.2 M Na_2SO_4	5.45	11.68	S10
Bi nanosheet array	0.1 M HCl	5.26	10.26	S11
S-Bi nanobelt	0.1 M Na_2SO_4	10.28	10.48	S12
edge-rich Bi NSs	0.10 M $NaHCO_3$	12.49	7.09	S13
Bi_2MoO_6	0.1 M HCl	20.46	8.17	S14
BiNi alloy	0.1 M Na_2SO_4	17.5	13.8	S15
Mosaic Bi nanosheets	0.1 M Na_2SO_4	13.23	10.46	S16
Ce-doped Bi_2WO_6	0.1 M HCl	22.5	15.90	S17
Bi nanoparticles	0.1 M HCl	20.80	11.50	S18

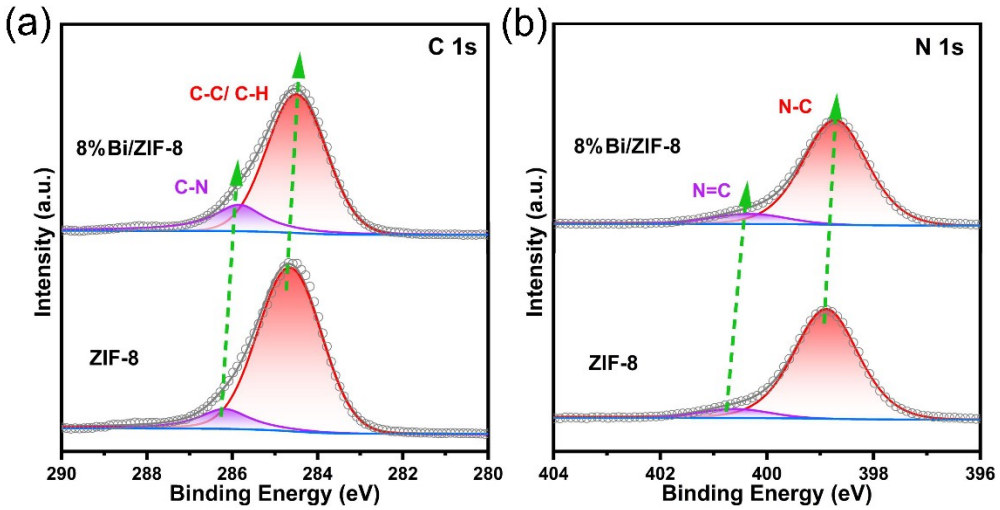

Fig. S1. (a) C 1s and (b) N 1s XPS spectra of ZIF-8 and 8%Bi/ZIF-8.

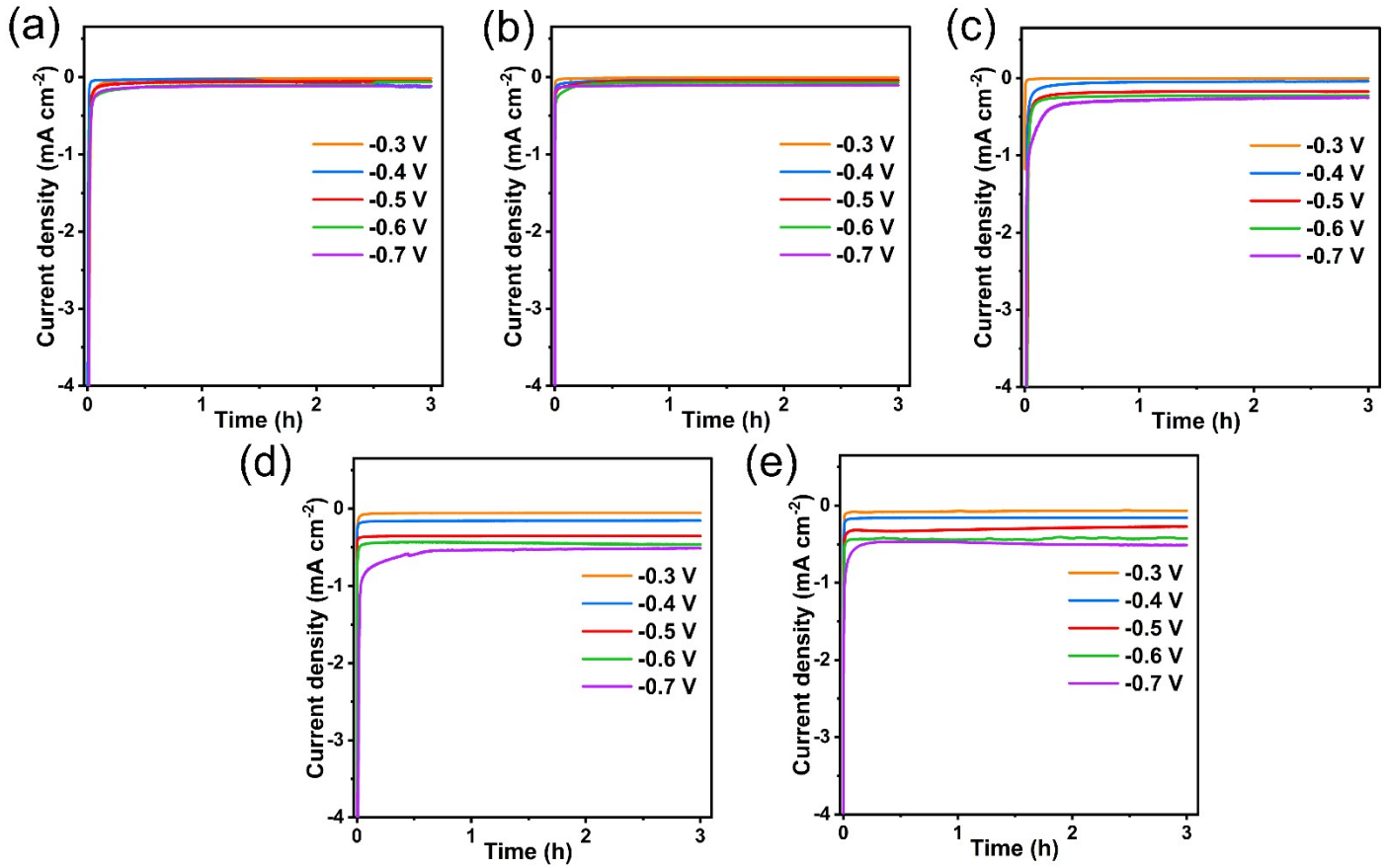

Fig. S2. *I-t* curves at different applied potentials in the N_2 filled states of (a) ZIF-8; (b) Bi NPs; (c) 4%Bi/ZIF-8; (d) 8%Bi/ZIF-8 and (e) 12%Bi/ZIF-8.

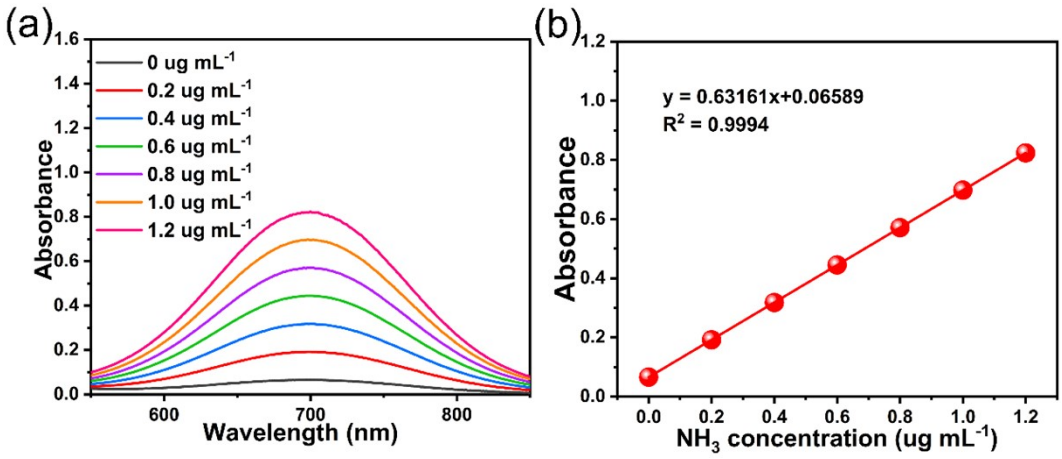

Fig. S3. In 0.1 mol L^{-1} Na_2SO_4, a specific concentration of NH_4Cl solution was used as the standard indophenol blue calibration curve. (a) UV-vis curves for the determination of indoxol at different ammonia concentrations after 1 hour of rest away from light and (b) calibration curves for determining NH_3 concentrations. The absorbance at 697 nm was measured by UV-vis spectrophotometer. The fitting curve showed a good linear correlation between absorbance and NH_3 concentration ($y = 0.63161x + 0.06589$, $R^2 = 0.9994$).

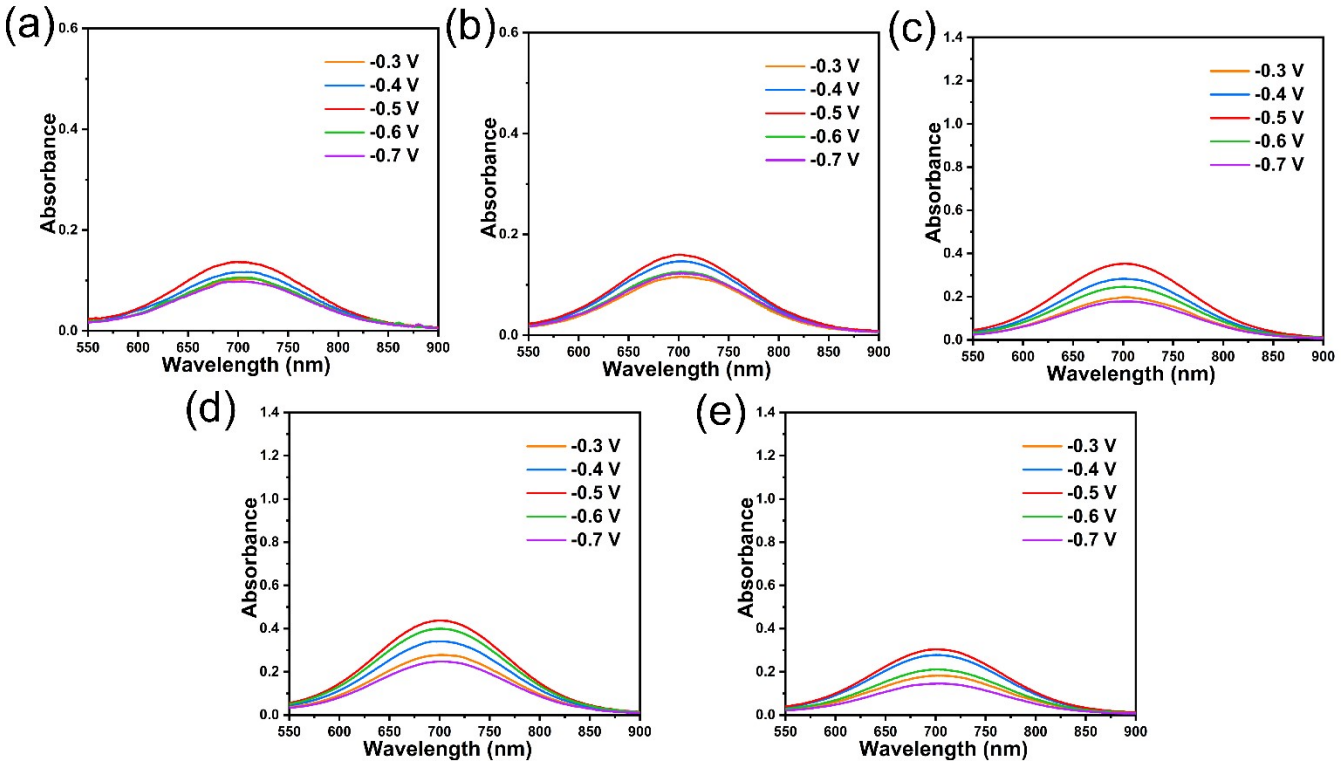

Fig. S4. UV-vis absorption spectra of the corresponding Ammonia absorbing solution after chronoamperometry tests for (a) ZIF-8; (b) Bi NPs; (c) 4%Bi/ZIF-8; (d) 8%Bi/ZIF-8 and (e) 12%Bi/ZIF-8.

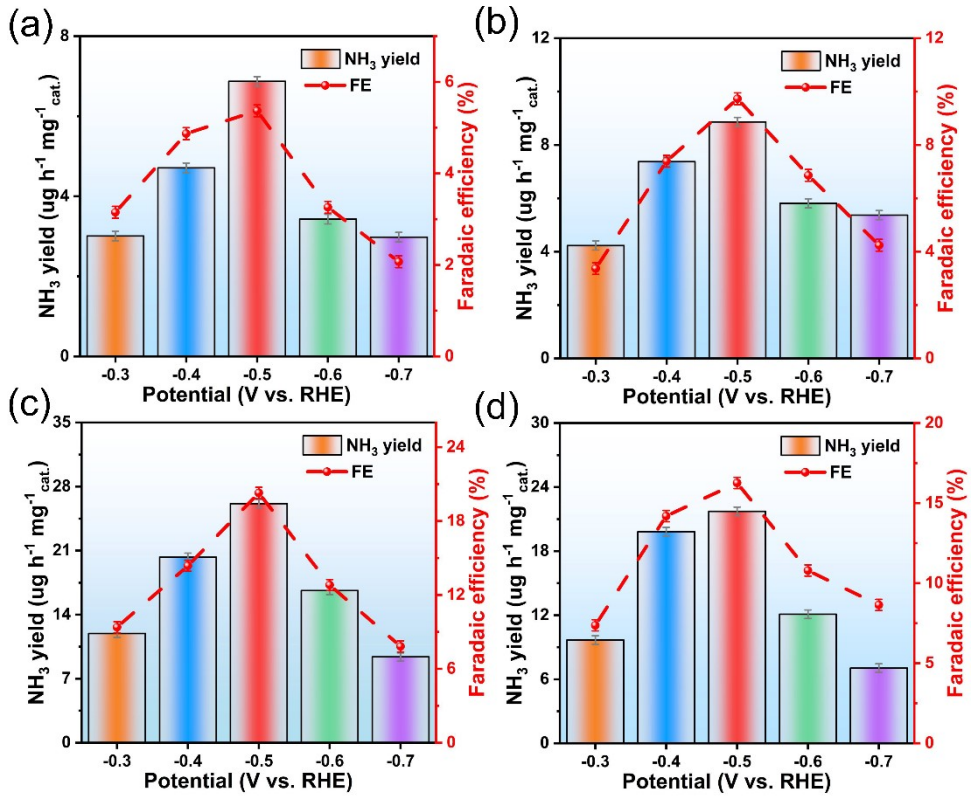

Fig. S5. The calculated NH_3 yield rate and FE at different applied potentials for (a) ZIF-8; (b) Bi NPs; (c) 4%Bi/ZIF-8 and (d) 12%Bi/ZIF-8.

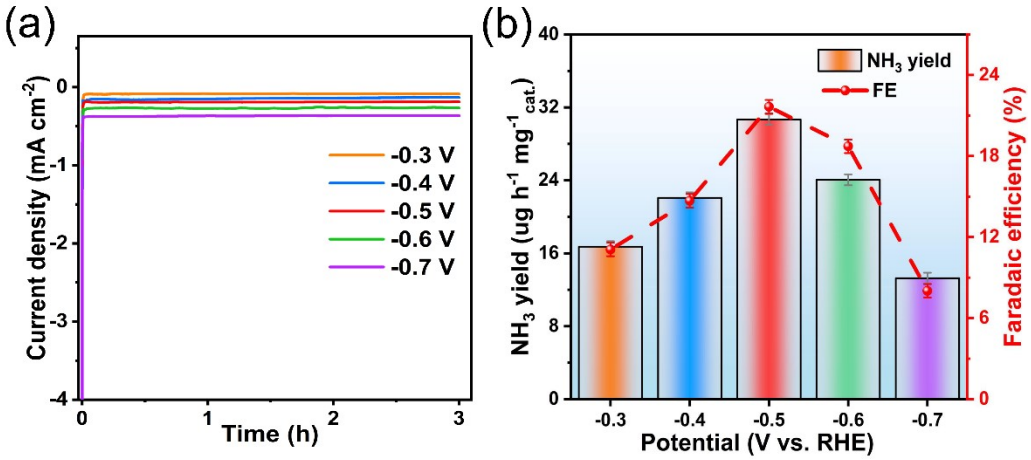

Fig. S6. (a) *I-t* curves in N_2-saturated electrolyte and (b) the corresponding NH_3 yield and FE of 6%Bi/ZIF-8 catalyst at different applied potentials.

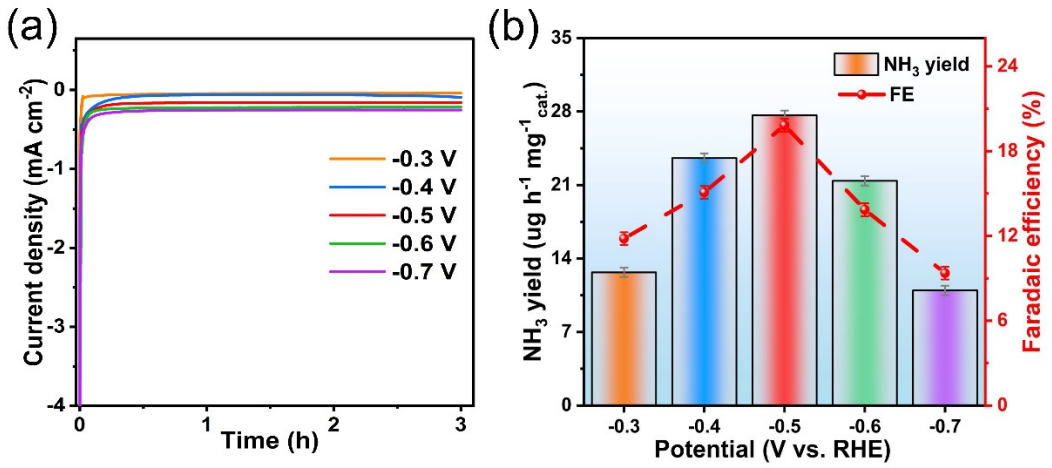

Fig. S7. (a) *I-t* curves in N_2-saturated electrolyte and (b) the corresponding NH_3 yield and FE of 10%Bi/ZIF-8 catalyst at different applied potentials.

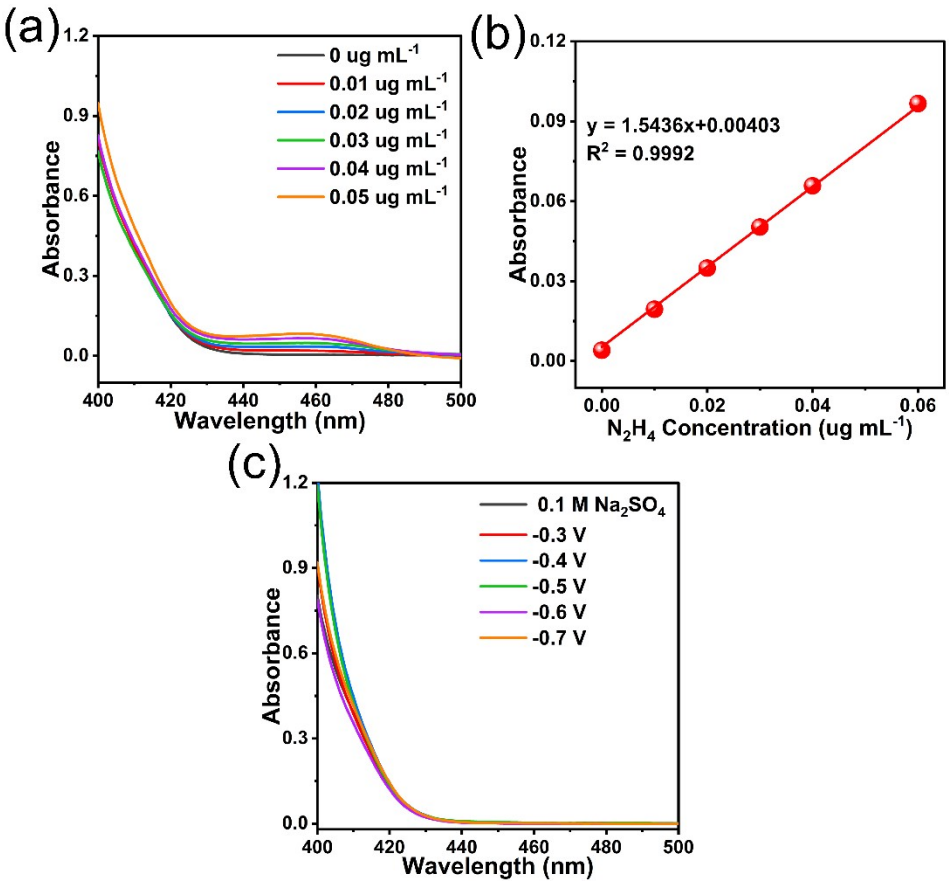

Fig. S8. Calibration test of N_2H_4. (a) UV-vis spectra of N_2H_4 solutions with different standard concentrations determined by Watt-Chrisp method; (b) Calibration curve of standard absorbance-N_2H_4 concentration; (c) UV-vis spectrum.

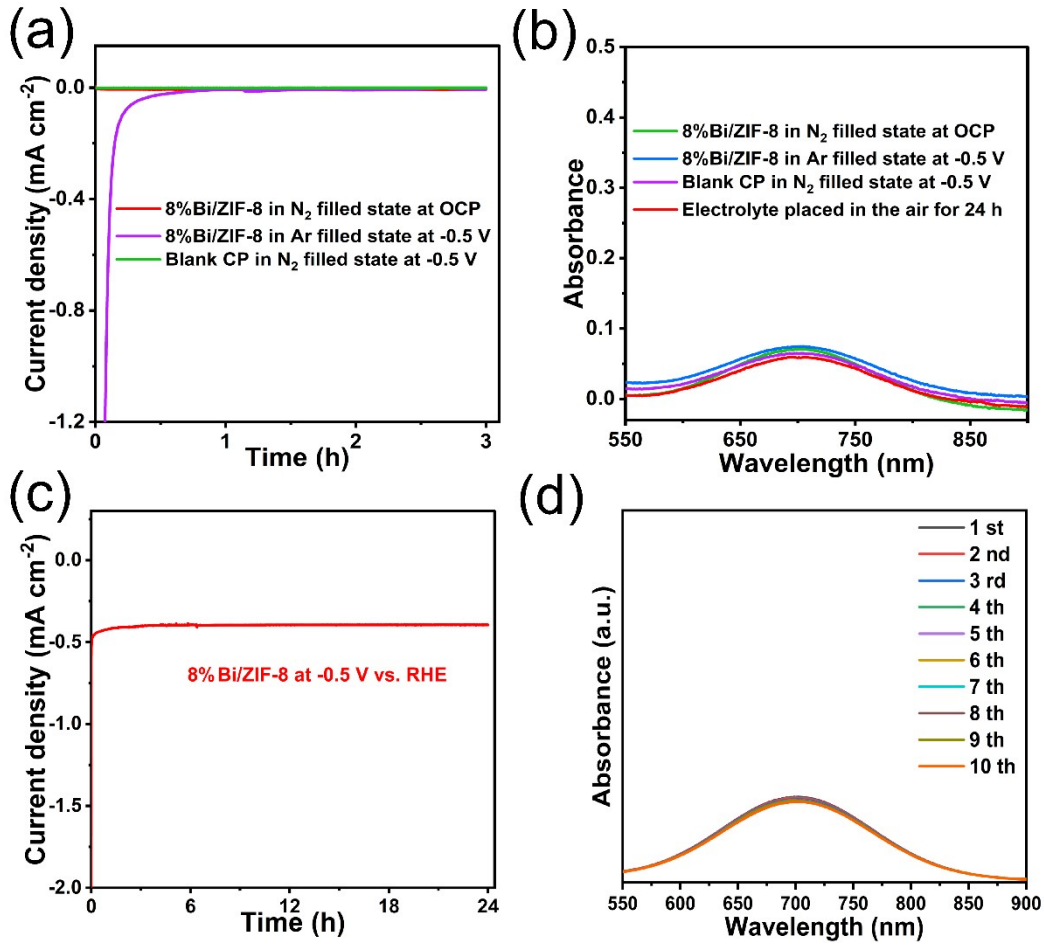

Fig. S9. (a) chronoamperometry curve and (b) UV-vis absorption spectra of the different control experiments; (c) the long-time chronoamperometry curves for 24 h and (d) UV-vis absorption spectra for ten cycles about 8%Bi/ZIF-8 catalyst.

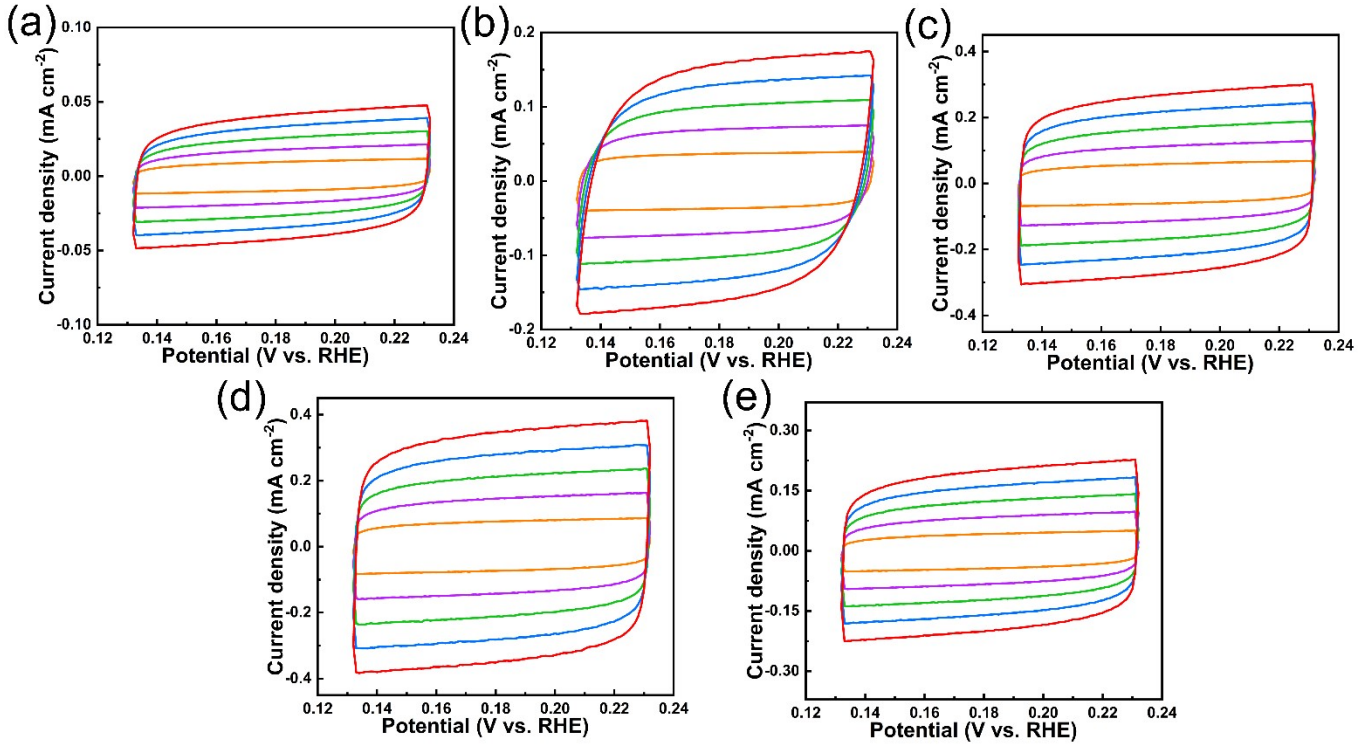

Fig. S10. CV curves without Faradic responses of (a) ZIF-8; (b) Bi NPs; (c) 4%Bi/ZIF-8; (d) 8%Bi/ZIF-8 and (e) 12%Bi/ZIF-8.

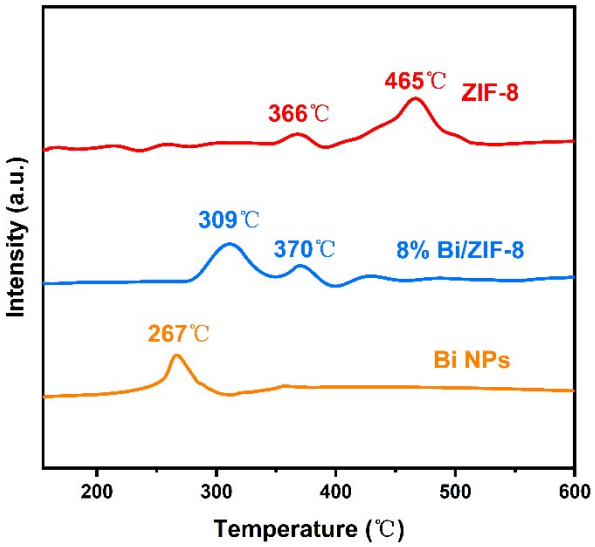

Figure S11. N_2-TPD curve

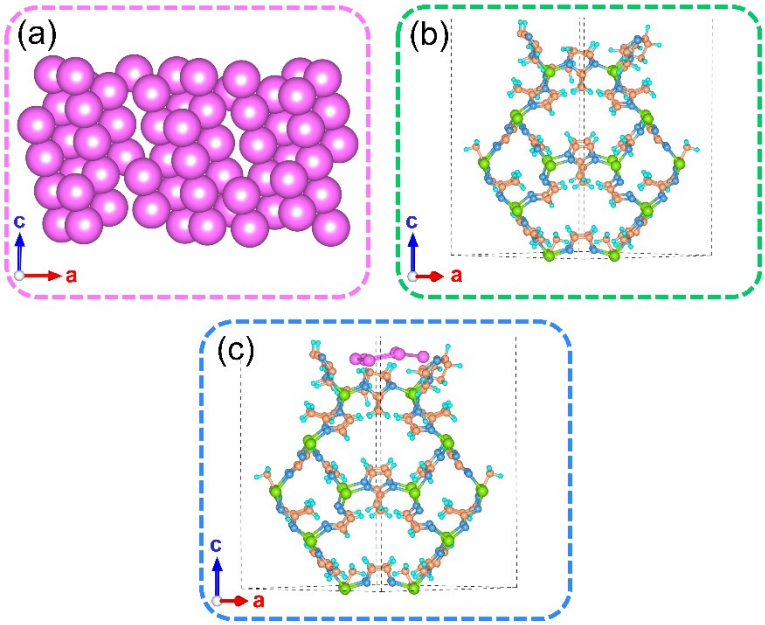

Fig. S12. The optimized structures of (a) Bi (110); (b) ZIF-8 and (c) Bi/ZIF-8 about front and top view.

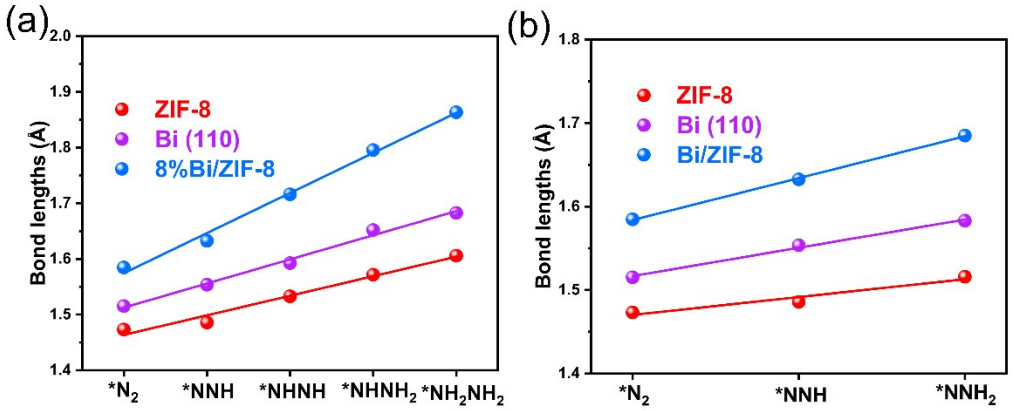

Fig. S13. Changes about N-N bond lengths of NRR on ZIF-8, Bi (110) and Bi/ZIF-8 surfaces through the (a) alternating and (b) distal pathways.

References

[S1] G. Kresse, J. Furthmüller, Efficiency of ab-initio total energy calculations for metals and semiconductors using a plane-wave basis set, Comp. Mater. Sci. 6 (1996) 15-50.

[S2] J.P. Perdew, K. Burke, M. Ernzerhof, Generalized gradient approximation made simple, Phys. Rev. Lett. 77 (1996) 3865-3868.

[S3] P.E. Blochl, Projector augmented-wave method, Phys. Rev. B Condens. Matter 50 (1994) 17953-17979.

[S4] S. Grimme, Semiempirical GGA-type density functional constructed with a long-range dispersion correction, J. Comput. Chem. 27 (2006) 1787-1799.

[S5] Y. Wan, H. Zhou, M. Zheng, Z. Huang, F. Kang, J. Li, R. Lv, Oxidation state modulation of bismuth for efficient electrocatalytic nitrogen reduction to ammonia, Adv. Funct. Mater. 31 (2021) 2100300.

[S6] F. Xu, F. Wu, K. Zhu, Z. Fang, D. Jia, Y. Wang, G. Jia, J. Low, W. Ye, Z. Sun, P. Gao, Y. Xiong, Boron doping and high curvature in Bi nanorolls for promoting photoelectrochemical nitrogen fixation, Appl. Catal. B Environ. 284 (2021)

119689.

[S7] B. Chang, Q. Liu, N. Chen, Y. Yang, A flower-like Bismuth oxide as an efficient, durable and selective electrocatalyst for artificial N_2 fixation in ambient condition, Chemcatchem 11 (2019) 1884-1888.

[S8] C. Lv, C. Yan, G. Chen, Y. Ding, J. Sun, Y. Zhou, G. Yu, An amorphous noble-metal-free electrocatalyst that enables nitrogen fixation under ambient conditions, Angew. Chem. Int. Ed. 57 (2018) 6073-6076.

[S9] J. Yao, D. Bao, Q. Zhang, M. Shi, Y. Wang, R. Gao, J. Yan, Q. Jiang, Tailoring oxygen vacancies of $BiVO_4$ toward highly efficient noble-metal-free electrocatalyst for artificial N_2 fixation under ambient conditions, Small Methods 3 (2019) 1800333.

[S10] Y. Wang, M. Shi, D. Bao, F. Meng, Q. Zhang, Y. Zhou, K. Liu, Y. Zhang, J. Wang, Z. Chen, D. Liu, Z. Jiang, M. Luo, L. Gu, Q. Zhang, X. Cao, Y. Yao, M. Shao, Y. Zhang, X. Zhang, J.G. Chen, J. Yan, Q. Jiang, Generating defect-rich bismuth for enhancing the rate of nitrogen electroreduction to ammonia, Angew. Chem. Int. Ed. 131 (2019) 9564-9569.

[S11] R. Zhang, L. Ji, W. Kong, H. Wang, R. Zhao, H. Chen, T. Li, B. Li, Y. Luo, X. Sun, Electrocatalytic N_2-to-NH_3 conversion with high faradaic efficiency enabled using a Bi nanosheet array, Chem. Commun. 55 (2019) 5263-5266.

[S12] Y. Lin, L. Yang, H. Jiang, Y. Zhang, Y. Bo, P. Liu, S. Chen, B. Xiang, G. Li, J. Jiang, Y. Xiong, L. Song, Sulfur atomically doped Bismuth nanobelt driven by electrochemical self-reconstruction for boosted electrocatalysis, J. Phys. Chem. Lett. 11 (2020) 1746-1752.

[S13] L. Xia, W. Fu, P. Zhuang, Y. Cao, M.O. Lam Chee, P. Dong, M. Ye, J. Shen, Engineering abundant edge sites of Bismuth nanosheets toward superior ambient

electrocatalytic nitrogen reduction via topotactic transformation, ACS Sustainable Chem. Eng. 8 (2020) 2735-2741.

[S14] Z. Xing, W. Kong, T. Wu, H. Xie, T. Wang, Y. Luo, X. Shi, A.M. Asiri, Y. Zhang, X. Sun, Hollow Bi_2MoO_6 sphere effectively catalyzes the ambient electroreduction of N_2 to NH_3, ACS Sustainable Chem. Eng. 7 (2019) 12692-12696.

[S15] Z. Fang, P. Wu, Y. Qian, G. Yu, Gel-derived amorphous bismuth-nickel alloy promotes electrocatalytic nitrogen fixation via optimizing nitrogen adsorption and activation, Angew. Chem. Int. Ed. 60 (2021) 4275-4281.

[S16] L. Li, C. Tang, B. Xia, H. Jin, Y. Zheng, S. Qiao, Two-dimensional mosaic bismuth nanosheets for highly selective ambient electrocatalytic nitrogen reduction, ACS Catal. 9 (2019) 2902-2908.

[S17] X. Yang, Y. Ma, Y. Liu, K. Wang, Y. Wang, M. Liu, X. Qiu, W. Li, J. Li, Defect-induced Ce-doped Bi_2WO_6 for efficient electrocatalytic N_2 reduction, ACS Appl. Mater. Interfaces 13 (2021) 19864-19872.

[S18] F. Wang, L. Zhang, T. Wang, F. Zhang, Q. Liu, H. Zhao, B. Zheng, J. Du, X. Sun, In situ derived Bi nanoparticles confined in carbon rods as an efficient electrocatalyst for ambient N_2 reduction to NH_3, Inorg. Chem. 60 (2021) 7584-7589.